Can destabilization rims of hydrous minerals be used to constrain magma ascent kinetics at lava dome volcanoes?

Lyderic France

Can destabilization rims of hydrous minerals be used to constrain magma ascent kinetics at lava dome volcanoes?

Bulletin of Volcanology (2020) 82:66

https://doi.org/10.1007/s00445-020-01405-4

Lydéric France

Université de Lorraine, CNRS, CRPG, F-54000 Nancy, France

*Corresponding author: lyderic.france@univ-lorraine.fr

Keywords:

biotite destabilization; trachyte lava; plumbing system; degassing; Chaîne des Puys; Sarcoui

Abstract

Time constraints on igneous processes related to eruption triggering, e.g., magma mixing or ascent in the conduit, are needed in any risk mitigation attempt. In this context, magma ascent rate and kinetics are key parameters as they may correspond to the response time available to civil protection during volcanic unrest. Several tools available to quantify such durations include diffusion chronometry, isotopic geochemistry, and hydrous mineral destabilization related to magma degassing during ascent through the conduit. Here I discuss the possible limitations of the widely used hydrous mineral destabilization chronometry applied to minerals within large lava bodies that cool relatively slowly (over days or weeks) such as thick lava flows and lava domes. Based on the type case of the Sarcoui dome (Chaîne des Puys, France) and its associated phreatomagmatic outbreak deposits, I suggest that hydrous mineral destabilization rims may, in some cases, develop at the surface during dome emplacement. From this perspective, preeruptive timescales calculated based on disequilibrium kinetics will be greatly underestimated, leading to a serious issue in the reconstruction of the eruption dynamics and its possible applications to emergency management for future eruptions. More generally, hydrous mineral destabilization chronometry should be used with great caution. Nevertheless, it remains a choice tool to quantify magma ascent rates for eruptions during which magmas quench upon arrival at the surface (e.g., Plinian, Vulcanian, or phreatomagmatic eruptions), with pumiceous textures being a good indicator of quenching. In the case of lava dome emplacement, I suggest that the minerals embedded in pumiceous clasts emitted during explosive phases are more reliable candidates for chronometry studies than crystals within the dome itself as those clasts might represent the fresh magma that triggered the explosion.

◦ *Introduction*

Understanding the mechanisms and quantifying the time scales and kinetics associated with volcanic unrest, eruption triggering, and magma ascent to the surface remain some of the holy grails of modern volcanology and igneous petrology. This has particular societal impact in the case of silica-rich magmas associated with the most explosive and destructive eruptions, for which risk mitigation requires such time constraints. In addition to the information provided by seismic and geophysical monitoring (e.g., Endo et al. 1981; Gudmundsson et al. 2014; Sigmundsson et al. 2014), igneous rocks record the various stages of their evolution, offering the potential for time constraints (e.g., Spiegelman & Elliott 1993; Rutherford 2008; Druitt et al. 2012). The main chronometric tools available are diffusion chronometry (e.g., Demouchy et al., 2006; Boudon et al. 2015; Shea et al. 2015; Ferguson et al., 2016; Costa et al., 2020), U-Th disequilibrium series (Girard et al. 2017), and mineral destabilization chronometry (Rutherford & Hill 1993; Faure et al., 2001; Browne & Gardner, 2006).

Since the pioneering study of Rutherford & Hill (1993), who quantified the ascent rate of Mount St. Helens dacite magmas in both dome forming eruptions, and large explosive Plinian to Subplinian eruptions, hundreds of studies have used their experimentally calibrated approach. Their method relies on the advancement of the destabilization reaction that affects hydrous minerals (e.g., pyroxene-oxide-plagioclase rims around amphibole) during magma degassing. Although initially calibrated for amphibole, similar destabilization reactions are reported for other hydrous minerals like biotite (Venezky & Rutherford, 1999; Underwood et al., 2012). This reaction is usually considered to occur during magma ascent as volatile solubility decreases dramatically upon decompression. Alternatively, it has been proposed and demonstrated experimentally that the reaction may occur when a more

primitive hotter magma intrudes a differentiated and partially cooled magma chamber (e.g., Feeley & Sharp, 1996; Plechov et al. 2008; De Angelis et al., 2015). Decompression-related dehydration drives hydrous minerals (e.g., amphibole or mica) to unstable conditions (Rutherford 2008), forming a reaction rim whose width is directly correlated to the duration between the onset of mineral destabilization and the final quenching of the lava. It is generally assumed that magmas are volatile saturated at mid-crustal or shallow magma chamber depths and that degassing starts as soon as magma begins its ascent (as an example, Métrich & Wallace, 2008). Thus, the depth of the magma chamber and the duration of degassing obtained from destabilization rims can be converted into an ascent or decompression rate. Nevertheless, volatile saturation of magmas at magma chamber depth should be demonstrated for each case study, as volatile-undersaturated melts would start to degas at shallower levels in the conduit, leading to over-estimated ascent rates. More generally any process with the potential to destabilize hydrous minerals should be carefully explored before proposing an ascent rate of magmas. As an example, during the cooling of large lava effusions or extrusions at the surface (e.g., thick lava flows or lava domes), the temperature of the lava may remain largely above the solidus temperature for several days or weeks (as an example, Dzurisin et al., 1990), enhancing the destabilization of hydrous minerals and prolonging the development of the destabilization rim (Garcia & Jacobson, 1979; Devine et al., 1998); such a process would lead to under-estimated ascent rates.

Based on the type case of the Sarcoui dome (Chaîne des Puys, France) destabilized biotite crystals, I show here that in some cases the destabilization rims may develop after magma ascent and during lava dome emplacement. I then explore more generally the utility of hydrous mineral destabilization rims in estimating the ascent rates of explosive and effusive or extrusive eruptions.

◦ *Geological context*

The Chaîne des Puys (CdP) is situated in the French Massif Central to the west of the Oligocene Limagne rift and borders the city of Clermont-Ferrand, a metropolitan area with ~480,000 inhabitants (Figure 1). The CdP is a 30-km-long north-south alignment of around a hundred monogenic cones, domes, and maars emplaced between ~100 and 6.7 ± 0.1 ka (Figure 1; Juvigne 1992; Boivin et al. 2009). French Massif Central magmatism is related to asthenospheric upwelling (Hoernle et al. 1995; Granet et al. 1995) and melting of a strongly metasomatized HIMU-type mantle (Lustrino & Wilson 2007; Hamelin et al. 2009; France et al. 2015; Gu et al. 2016, 2018; the HIMU isotopic signature likely documenting the influence of a recycled component in the mantle source, Zindler & Hart, 1986). Volatile- and silica-rich magmas, like the trachyte lavas forming the Sarcoui edifice studied herein (~12.5 ± 0.5 ka; Miallier et al. 2017), formed through protracted differentiation, and ~5%–10% crustal contamination (Villemant et al. 1980; Condomines et al. 1982; Hamelin et al. 2009; Martel et al. 2013; France et al. 2016). Recently, it has been proposed that the CdP plumbing system may still contain some residual melt, although any potential eruption would require an unlikely mush rejuvenation (France et al. 2016) as described for large silicic eruptions (Bachmann & Bergantz, 2003; Hubert et al., 2010).

Sarcoui volcano is a lava dome of ca. 1 km in diameter and of ca. 150 m high; it is composed of massive trachyte lava containing biotite and alkali feldspar phenocrysts (whole-rock compositions available in Martel et al. 2013; Table 1). The lava dome has suffered several destabilization events and is bordered by several block-and-ash deposits (BAD) that are locally buried below massive trachyte lavas, highlighting that destabilization occurred during dome growth (Miallier et al. 2017).

◦ *Methods*

Field work was conducted to reconstruct the stratigraphy, field relations between the various facies, and sample the key lithologies. Major element mineral compositions and backscattered electron images (BSE) were determined using a CAMECA SX100 electron probe (SCMEM; Université de Lorraine, France) equipped with five spectrometers and the "Peak sight" operating system. Data were obtained using a 12 kV acceleration potential, a static (fixed) beam, Kα emissions from all elements, and a matrix correction based on Pouchou & Pichoir (1991). Crystals were analyzed with a beam current of 10 nA, a focused beam, and counting times of 20 s on background and 40 s on peak.

◦ *Results: Stable and destabilized biotite at Sarcoui volcano*

Field evidence of an initial explosive phase followed by lava dome emplacement

At various outcrops located in the two northeast quarries, pyroclastic deposits are recognized below the dome deposits (Figure 2), and attest of an initial explosive phase for which fragmentation could have been phreatomagmatic. Samples for the present study were collected in two old quarries (45°48'54.4"N, 2°59'15.9"E, and 45°48'58.9"N, 2°59'09.9"E; Table S1). Both outcrops contain dark and roundish, relatively dense (in comparison to the massive dome trachyte lava) trachyte lapilli and blocks with a quenched aspect that can be classified as cauliflower bombs (Figures 2a, b). Also present are angular accidental blocks of basalt and gneiss (full thin sections presented in Figures 2c and d, respectively) embedded in an ash matrix. Most of the trachyte lapilli and blocks display a banded texture with vesicle-poor and -rich bands that seems to preserve conduit-related shearing (Shea et al. 2012; France et al. 2016). The characteristics of the pyroclastic deposits

136 related to this initial explosive phase, and more specifically the presence of cauliflower
137 bombs, and of angular accidental blocks of basalt and gneiss embedded in an ash matrix
138 suggest that the fragmentation could have been phreatomagmatic. Although the origin of
139 fragmentation should be considered with caution (White & Valentine, 2016), based on those
140 evidences, and relying on previous volcanological studies in the Chaîne des Puys area (e.g.,
141 De Goer et al., 1992; Miallier et al., 2004; Boivin et al., 2009), I will hereafter name this
142 pyroclastic unit "phreatomagmatic deposits". This phreatomagmatic deposit may
143 correspond to units SU2 and SU3 from Miallier et al. (2017), although they did not identify
144 the accidental angular and fragmented material. Similar to their observations, no paleosol or
145 erosion features have been observed between the phreatomagmatic deposits and the
146 overlying dome lavas or pyroclastic density currents related BADs (Figure 2).
147 Thermoluminescence dating of the phreatomagmatic deposits, and ^{238}U-^{230}Th dating of
148 dome samples give similar ages (12.6 ± 3 ka, and 12.8 ± 1.4 ka, respectively, 2σ errors;
149 Miallier et al. 2004). Field evidence and geochronology therefore support a model in which
150 the phreatomagmatic stage represents the initial breakout that was directly followed by
151 dome emplacement, in agreement with early detailed field studies (De Goër et al. 1991).
152
153 ***Petrography and phase compositions***
154 The similar mineral assemblages and the perfect match of mineral compositions of
155 the dome and initial phreatomagmatic products presented below, highlight that both
156 eruptive phases were fed by the same trachyte magma. Both trachyte magmas display
157 porphyritic textures with 5 to 10% phenocrysts of plagioclase (2 × 0.6 mm) and biotite (~1.5
158 mm) with no difference observed between the phenocryst fraction of dome and
159 phreatomagmatic samples (point counting estimates). Martel et al. (2013) showed that this

mineral assemblage in the Sarcoui magma had an equilibrium temperature of ~800°C. Plagioclase is zoned, and biotite displays skeletal morphologies (Figure 3). The matrix is composed of microlites of plagioclase with potassic feldspar rims, biotite, and iron oxide. Microphenocrysts (~100 µm) of apatite and zircon are recognized throughout the matrix and included in the biotite and plagioclase phenocrysts. Crystallites, the smallest microlites, are also similar in composition and assemblage (potassic feldspar, biotite, and iron oxide) between the dome and phreatomagmatic samples, but are ~2 times larger in dome samples. Phenocrysts and microlites are oriented in the same direction in all samples; in the cauliflower bombs, this highlights that the larger microlites had already crystallized when the trachyte magma was migrating through the conduit. Crystallites are only locally oriented. In dome samples, all biotite crystals are rimmed by dark, oxide-rich, in average 20 µm large destabilization coronas that contain potassic feldspar, Ti-magnetite, plagioclase, and rare ilmenite (Figures 3, 4). Only rare Mg-rich clinopyroxene is present suggesting that in a similar way as for amphibole destabilization, the reaction is not equilibrated, and thus have likely proceeded with melt present (Rutherford & Hill, 1993). Several examples of reaction rims are presented in Figure 4 along with an attempt of mass balance based on compositions presented in Table 1. The estimated reaction is 0.5 biotite + 0.5 melt => 0.63 K-feldspar + 0.18 titanomagnetite + 0.12 plagioclase + 0.04 clinopyroxene + 0.03 ilmenite + $melt_2$ (with $melt_2$ enriched in both Mg and K, and depleted in Fe). Similar to the pioneering work of Rutherford & Hill (1993), the mass balance residuals are relatively high, suggesting that the reaction proceeded with melt present before and after an increment of reaction. In contrast, no destabilization features are observed in phreatomagmatic samples (Figure 3). The matrices of phreatomagmatic samples contain micro-vesicle-rich and -poor bands, consistent with the low densities of the bombs (1.5-2 g/cm^3; France et al. 2016; Miallier et al.

184 2017), whereas dome sample matrices contain widespread vesicles, consistent with the
185 lower densities locally observed in the dome lavas (~1.3 g/cm^3; France et al. 2016; Miallier et
186 al. 2017).

187 Mineral compositions are very similar in the dome and phreatomagmatic samples
188 (Figure 5). Biotite contains 5.5 wt% TiO_2, 14 wt% Al_2O_3, and 12.5 wt% MgO with no
189 compositional difference between the massive dome trachyte lava and the dense cauliflower
190 bombs (Table 1). Feldspar compositions (Figure 5; Table 1) vary from andesine ($An_{31}Ab_{64}Or_5$)
191 to alkali feldspar ($An_1Ab_{49}Or_{50}$). Phenocryst cores are more Ca-rich (andesine to oligoclase)
192 than microlite and crystallite cores (oligoclase to anorthoclase). The rims of all feldspar
193 grains display more evolved compositions that range from Or_{33} to Or_{50}.

194 Oxygen isotopes measured in zircon grains record crustal contamination at magma
195 chamber depth, but display no variation between the dome and phreatomagmatic samples
196 (France et al. 2016).

197

198 ◦ ***Discussion***

199 ***Development of biotite destabilization rims at Sarcoui lava dome***

200 The various petrographic and geochemical features described herein and in the
201 literature show that the same magma, which experienced similar magma chamber and
202 conduit processes, is responsible for the dome and phreatomagmatic eruptions at Sarcoui.
203 Those various results highlight that the lava dome was emplaced immediately after the
204 phreatomagmatic outbreak. To summarize, these main features are: 1) the lack of a paleosol
205 between the phreatomagmatic deposits and dome ones (dome lavas or BAD; Figure 2); 2)
206 the similar ages between the two facies; 3) the similar mineral cargo charges, and thus a
207 similar influence on magma viscosity; and 4) the identical phase compositions of phenocrysts

that document magma chamber processes, microlites that seem to document conduit processes, and crystallites that document the very last stages of crystallization at or near the surface (Figure 5). The strong similarity in crystal proportion and mineral composition down to the smaller crystallites implies that each of the various generations of crystals crystallized in similar conditions and from similar melts during the dome and phreatomagmatic stages. Although the density of dome trachyte lavas varies slightly due to their micro-vesicularity that developed late during dome emplacement, both dome and phreatomagmatic samples are relatively dense and incipiently to poorly vesicular according to Houghton & Wilson (1989) classification (e.g., no pumice texture observed). In the case of the initial phreatomagmatic stage, this implies that most of the eruption's explosive energy came from water-magma interaction, and not from 'dry' explosive magma fragmentation. Therefore, the only difference between the phreatomagmatic and dome-extrusion phases was the duration of shallow crystallization (or rate of cooling), which was long (slow) for dome lavas and short (quenched) for phreatomagmatic samples, consistent with the biotite-destabilization rims and larger crystallites observed in the dome samples. These different emplacement modes are related to an external parameter: the presence (phreatomagmatic outbreak stage) or lack (dome stage) of a water table or abundant infiltrated basement fluids that could trigger phreatomagmatic fragmentation when the magma:water ratio is optimal (White & Valentine, 2016). Consequently, there is no indication of any difference between the phreatomagmatic and dome stages prior to the water-magma interaction, and similar ascent conditions are therefore likely. In that case, most, if not all, of the biotite destabilization rims are related to destabilization at depths shallower than the melt-water interactions of the phreatomagmatic stage, and thus very close to the surface or during dome emplacement. Similar conclusions were reached for some destabilization rims of

amphibole at Soufriere Hill, and in the Cascades (Garcia & Jacobson, 1979; Devine et al., 1998). This also implies that a relatively quick conduit ascent should be considered for both the phreatomagmatic and dome stages with striking implications for risk mitigation. However, the ascent rate cannot yet be quantified, as only amphibole destabilization experiments are available; none have been reported for biotite. Once the kinetics of biotite destabilization upon magma ascent, or at surface conditions will be quantified with future experiments, the biotite destabilization rims in dome samples may be used to obtain minimum ascent rates, and an overall cooling rate of the dome lava. As a comparison, a lack of destabilization rim for amphibole crystals would document an ascent of magmas from reservoir to surface in less than 4 days, when a 20 µm destabilization rim would develop in a lava dome at surface conditions in tens of days (Rutherford & Hill, 1993). According to Underwood et al. (2012) biotite destabilization is likely to develop faster than amphibole destabilization due to the higher diffusivity of H in biotite, suggesting that those duration estimates would be maximum values. Those authors also documented that biotite and amphibole are more extensively reacted in the core of the Lassen Peak dome (US) where cooling rates are lower than in its external parts, suggesting that the development of destabilization rims at surface conditions is not restricted to Sarcoui dome, and should be seriously considered in any study.

General implications and conclusions

The results described herein support a model in which magma ascent conditions in the conduit were similar for the phreatomagmatic (prior to water-magma interaction) and dome-extrusion phases at Sarcoui. It is therefore likely that the biotite destabilization rims observed exclusively in dome samples developed during dome emplacement, and should not

256 be used to quantify trachyte magma ascent rates in the conduit. If those were mistakenly
257 used for purposes of ascent kinetics estimates, the latter would be greatly underestimated,
258 implicating serious issues in the development of risk mitigation plans. My results suggest
259 that the approach of Rutherford & Hill (1993) should be applied with caution when
260 considering samples that may have cooled slowly (days to weeks) at the surface, e.g., thick
261 lava flows, domes, and lava lakes. Samples that quenched upon arrival at the surface, i.e.,
262 juvenile ejecta from explosive eruptions (scoria, pumice, phreatomagmatic bombs),
263 nevertheless remain perfectly suitable to apply this method. Dome samples are not always
264 unsuited to this method, but a detailed petrographic study is required to prove that
265 destabilization rims formed during magma ascent through the conduit and not during dome
266 emplacement at the surface. To apply Rutherford & Hill's (1993) method to domes, it seems
267 that the best samples are those that are strongly vesiculated and associated with dilute
268 pyroclastic density currents (PDCs; e.g., explosive dome eruptions), as they represent the
269 quenching of fresh magma injected within the dome and the triggering of the explosive
270 eruption (Boudon et al. 2015). This was for example the case for strongly vesiculated
271 pyroclasts from BAD related to PDC from the 1991-1995 Unzen eruption (Holtz et al., 2005;
272 Browne et al., 2006). There destabilization rims can confidently be attributed to magma
273 mixing or destabilization upon ascent, and may be used as chronometers. One striking
274 difference between Unzen volcano biotite destabilization rims, and the ones studied herein
275 is the presence of amphibole as a destabilization product at Unzen (Browne et al., 2006). As
276 initially suggested by Feeley & Sharp (1996), the presence of amphibole may thus represent
277 an indicator or rims formed upon ascent by opposition to rims formed at surface during
278 dome cooling like in the present study where such a hydrous mineral is lacking. This will
279 nevertheless have to be confirmed by future experimental constraints. Less-vesiculated and

rather degassed magmas associated with PDCs may rather represent the slowly cooled and degassed rigid dome carapace that fragments during the explosive eruption (Boudon et al. 2015), and should not be used.

Acknowledgments:

Mickael Demacon is thanked for numerous discussions related to the various processes involved in Sarcoui trachyte magma genesis and evolution during his undergraduate project. François Faure is thanked for assistance during field sampling. Georges Boudon is thanked for discussions related to estimating the kinetics of igneous processes in silica-rich systems. I thank the Editor, two anonymous reviewers, and Pavel Plechov for constructive comment that improved the manuscript. This is CRPG contribution n°XXXX.

References:

Bachmann O, Bergantz GW (2003) Rejuvenation of the Fish Canyon magma body: A window into the evolution of large-volume silicic magma systems. Geology, 31, 789–792.

Boivin P, Besson JC, Briot D, Camus G, Goer De Herve A, Gourgaud A, Labazuy P, Langlois E, Larouzière FD, Livet M, Mergoil J, Miallier D, Morel JM, Vernet G, Vincent PM, (2009) Volcanologie de la Chaîne des Puys, Massif Central Français. Parc Naturel Régional des Volcans d'Auvergne Clermont-Ferrand, 196 p, 1/25 000 map.

Boudon G, Balcone-Boissard H, Villemant B, Morgan DJ (2015) What factors control superficial lava dome explosivity? Sci Rep 5: 14551. doi: 10.1038/srep14551

Browne BL, Gardner JE (2006) The influence of magma ascent path on the texture, mineralogy, and formation of Hornblende reaction rims. Earth Planet. Sci. Lett. 246: 161–176.

Browne BL, Eichelberger JC, Patino LC, Vogel TA, Dehn J, Uto K, Hoshizumi H (2006) Generation of porphyritic and equigranular mafic enclaves during magma recharge events at Unzen volcano, Japan. J Petrol 47-2: 301-328. doi:10.1093/petrology/egi076

Condomines M, Morand P, Camus G, Duthou L (1982) Chronological and geochemical study of lavas from the Chaîne des Puys, Massif Central, France: evidence for crustal contamination. Contrib Mineral Petrol 81: 296–303.

Costa F, Shea T, Ubide T (2020) Diffusion chronometry and the timescales of magmatic processes. Nature Reviews-Earth & Environment 1: 201-214. doi:10.1038/s43017-020-0038-x

De Angelis SH, Larsen J, Coombs M, Dunn A, Hayden L (2015) Amphibole reaction rims as a record of pre-eruptive magmatic heating: An experimental approach. Earth and Planetary Science Letters 426: 235-245

313 De Goër A, Camus G, Gourgaud A, Kieffer G, Mergoil J, Vincent P (1991) Volcanologie de la Chaîne des
314 Puys. Parc Naturel Régional des Volcans d'Auvergne Edition, 128pp.

315 Demouchy S, Jacobsen SD, Gaillard F, Stern CR (2006) Rapid magma ascent recorded by water
316 diffusion profiles in mantle olivine. Geology 34-6: 429-432. doi:10.1130/G22386.1

317 Devine JD, Rutherford MJ, Gardner JE (1998) Petrologic determination of ascent rates for the 1995-
318 1997 Soufriere Hills volcano andesitic magma. Geophysical Research Letters 25-19: 3673-3676

319 Druitt TH, Costa F, Deloule E, Dungan M, Scaillet B (2012) Decadal to monthly timescales of magma
320 transfer and reservoir growth at a caldera volcano. Nature 482: 77-80.
321 doi:10.1038/nature10706Dzurisin D, Denlinger RP, Rosenbaum JG (1990) Cooling rate and
322 thermal structure determined from progressive magnetization of the Dacite Dome at Mount
323 St. Helens, Washington. J. Geophys. Res. 95, 2763. doi:10.1029/JB095iB03p02763

324 Endo ET, Malone SD, Noson LL, Weaver CJ (1981) Locations, magnitudes and statistics of the March
325 20--May 18 earthquake sequence. USGS Prof. Pap. 1250: 93-108.

326 Faure F, Trolliard G, Montel JM, Nicollet C (2001) Nano-petrographic investigation of a mafic xenolith
327 (maar de Beaunit, Massif Central, France). Eur. J. Mineral. 13: 27-40.

328 Feeley TC, Sharp ZD (1996) Chemical and hydrogen isotope evidence for in situ dehydrogenation of
329 biotite in silicic magma chambers. Geology 24-11: 1021-1024.

330 Fergusson DJ, Gonnermann HM, Ruprecht P, Plank T, Hauri EH, Houghton BF, Swanson DA (2016)
331 Magma decompression rates during explosive eruptions of Kilauea volcano, Hawaii, recorded
332 by melt embayments. Bull Volcanol 78: 71. doi:10.1007/s00445-016-1064-x

333 France L, Chazot G, Kornprobst J, Dallai L, Vannucci R, Grégoire M, Bertrand H, Boivin P (2015) Mantle
334 refertilization and magmatism in old orogenic regions: the role of late-orogenic pyroxenites.
335 Lithos 232: 49–75. http://dx.doi.org/10.1016/j.lithos.2015.05.017

336 France L, Demacon M, Gurenko A, Briot D (2016) Oxygen isotopes reveal crustal contamination and a
337 large, still partially molten magma chamber in Chaîne des Puys (French Massif Central). Lithos
338 260: 328–338.

339 Garcia MO, Jacobson SS (1979) Crystal clots, amphibole fractionation and the evolution of calc-
340 alkaline magmas. Contrib Mineral Petrol 69: 319-327

341 Girard G, Reagan MK, Sims KWW, Thornber CR, Waters CL, Phillips EH (2017) ^{238}U-^{230}Th-^{226}Ra-^{210}Pb-
342 ^{210}Po Disequilibria Constraints on Magma Generation, Ascent, and Degassing during the
343 Ongoing Eruption of Kīlauea. J Petrol 58-6: 1199–1226. doi:10.1093/petrology/egx051

344 Gudmundsson A, Lecoeur N, Mohajeri N, Thordarson T (2014) Dike emplacement at Bardarbunga,
345 Iceland, induces unusual stress changes, caldera deformation, and earthquakes. Bull Volcanol
346 76: 869.

347 Granet M, Wilson M, Achauer U (1995) Imaging a plume beneath the French Massif Central. Earth
348 Planet Sci Lett 136: 281–296.

349 Gu X, Deloule E, France L, Ingrin J (2016) Multi-stage metasomatism revealed by trace element and Li
350 isotope distributions in minerals of peridotite xenoliths from Allègre volcano (French Massif
351 Central). Lithos 264: 158–174.

352 Gu X, Ingrin J, Deloule E, France L, Xia Q (2018) Metasomatism in the sub-continental lithospheric
353 mantle beneath the south French Massif Central: Constraints from trace elements, Li and H in
354 peridotite minerals. Chem Geol 478: 2-17. doi:10.1016/j.chemgeo.2017.08.006

355 Hamelin C, Seitz HM, Barrat JA, Dosso L, Maury RC, Chaussidon M (2009) A lowδ^7Li lower crustal
356 component: evidence from an alkalic intraplate volcanic series (Chaîne des Puys, French Massif
357 Central). Chem Geol 266: 205–217.

358 Hoernle K, Zhang YS, Graham D (1995) Seismic and geochemical evidence for large scale mantle
359 upwelling beneath the eastern Atlantic and western and central Europe. Nature 374: 34–39.

Holtz F, Sato H, Lewis J, Behrens H, Nakada S (2005) Experimental petrology of the 1991–1995 Unzen dacite, Japan. Part 1: Phase relations, phase composition, and pre-eruptive conditions. Journal of Petrology 46, 319–337.

Houghton BF, Wilson CJN (1989) A vesicularity index for pyroclastic deposits. Bull Volcanol 51: 451-462

Huber C, Bachmann O, Manga M (2010) Two competing effects of volatiles on heat transfer in crystal-rich magmas: Thermal insulation vs defrosting. J Petrol 51: 847–867

Juvigne E (1992) Studies on the age of two volcanic lacustrine craters of Auvergne (France). Comptes Rendus Acad Sci Série 2-314: 401–404.

Lustrino M, Wilson M (2007) The Circum-Mediterranean Anorogenic Cenozoic Igneous Province. Earth Sci Rev 81: 1–65.

Martel C, Champallier R, Prouteau G, Pichavant M, Arbaret L, Balcone-Boissard H, Boudon G, Boivin P, Bourdier JL, Scaillet B (2013) Trachyte phase relations and implication for magma storage conditions in the Chaîne des Puys (FrenchMassif Central). J Petrol 54-6: 1071–1107. http://dx.doi.org/10.1093/petrology/egt006.

Métrich N, Wallace P (2008) Volatile abundances in basaltic magmas and their degassing paths tracked by melt inclusions. In: Putirka K, Tepley F (eds) Minerals, Inclusions and Volcanic Processes. Mineralogical Society of America, Reviews in Mineralogy and Geochemistry 69: 363-402.

Miallier D, Condomines M, Pilleyre T, Sanzelle S, Guittet J (2004) Concordant thermoluminescence and ^{238}U–^{230}Th ages for a trachytic dome (Grand Sarcoui) from the Chaîne des Puys (French Massif Central). Quat Sci Rev 23-5/6: 709–715.

382 Miallier D, Pilleyre T, Boivin P, Labazuy P, Gailler LS, Rico J (2017) Grand Sarcoui volcano (Chaîne des
383 Puys, Massif Central, France), a case study for monogenetic trachytic lava domes. J Volcanol
384 Geotherm Res 345: 125–141. doi: 10.1016/j.jvolgeores.2017.07.015

385 Plechov PY, Tsai AE, Shcherbakov VD, Dirksen OV (2008) Opacitization conditions of hornblende in
386 Bezymyannyi volcano andesites (March 30, 1956 Eruption). Petrology 16-1: 21-37.

387 Pouchou JL, Pichoir F (1991) Quantitative analysis of homogeneous or stratified microvolumes
388 applying the model ‘‘PAP’’. In: Heinrich KFJ, Newbury DE (eds) Electron Probe Quantification,
389 Plenum, New York, pp 31–75.

390 Rutherford MJ (2008) Magma ascent rates. Rev Mineral Geochem 69: 241–271.

391 Rutherford MJ, Hill PM (1993) Magma ascent rates from amphibole breakdown: Experiments and the
392 1980-1986 Mount St. Helens eruptions. J Geophys Res 98: 19667-19685.

393 Shea T, Gurioli L, Houghton BF (2012) Transitions between fall phases and pyroclastic density
394 currents during the AD 79 eruption at Vesuvius: building a transient conduit model from the
395 textural and volatile record. Bull Volcanol 74: 2363–2381.

396 Shea T, Costa F, Krimer D, Hammer JE (2015) Accuracy of timescales retrieved from diffusion
397 modeling in olivine: A 3D perspective. Am Mineral 100: 2026-2042.

398 Sigmundsson F, Hooper A, Hreinsdòttir S, Vogfjörd KS, Òfeigsson BG, Heimisson ER, Dumont S, Parks
399 M, Spaans K, Gudmundsson GB, Drouin V, Àrnadòttir T, Jònsdòttir K, Gudmundsson MT,
400 Högnadòttir T, Fridriksdòttir HM, Hensch M, Einarsson P, Magnùsson E, Samsonov S,
401 Brandsdòttir B, White RS, Àgùstsdòttir T, Greenfield T, Green RG, Hjartardòttir AR, Pedersen R,
402 Bennett RA, Geirsson H, La Femina PC, Björnsson H, Pàlsson F, Sturkell E, Bean CJ, Möllhoff M,
403 Braiden AK, Eibl EPS (2014) Segmented lateral dyke growth in a rifting event at Bàrðarbunga
404 volcanic system, Iceland. Nature 517: 191-195. doi:10.1038/nature14111

405 Spiegelman M, Elliott T (1993) Consequences of melt transport for uranium series disequilibrium in
406 young lavas. Earth Planet Sci Lett 118-1/4: 1-20

407 Underwood SJ, Feeley TC, Clynne MA (2012) Hydrogen isotope investigation of amphibole and biotite
408 phenocrysts in silicic magmas erupted at Lassen volcanic center, California. Journal of
409 Volcanology and Geothermal Research 227-228: 32-49

410 Venezky DY, Rutherford MJ (1999) Petrology and Fe–Ti oxide reequilibration of the 1991 Mount
411 Unzen mixed magma. Journal of Volcanology and Geothermal Research 89: 213–230

412 Villemant B, Joron JL, Jaffrezic H, Treuil M, Maury RC, Brousse R (1980) Cristallisation fractionnée
413 d'un magma basaltique alcalin: la série de la Chaîne des Puys (Massif Central, France). II.
414 Géochimie. Bull Mineral 103: 267–286.

415 White JDL, Valentine GA (2016) Magmatic versus phreatomagmatic fragmentation: Absence of
416 evidence is not evidence of absence. Geosphere 12-5: 1478–1488. doi:10.1130/GES01337.1

417 Zindler A, Hart, SR (1986) Chemical geodynamics. Annu. Rev. Earth Planet. Sci.

418

Figure captions:

Figure 1: Simplified maps of the study area modified after France et al. (2016). The location of Chaîne des Puys in France is shown, and the location and geological map of Sarcoui volcano is presented (from Boivin et al. 2009). Red arrows and asterisks document the block and ash deposit location and flow directions. Numbers in rectangles refers to the determined ages.

Figure 2: Characteristics of the phreatomagmatic outcrops from the NE quarries of Sarcoui dome (Figure 1). The reddish ash and cauliflower bombs characteristic of a phreatomagmatic deposit (a-b) is overlaid by a block-and-ash deposit (BAD) characteristic of the Sarcoui dome pyroclastic density currents (PDC). Note in a) the lack of any paleosol in between phreatomagmatic deposit and the Sarcoui dome related BAD. c) and d) present full thin section images of accidental clasts that are part of the phreatomagmatic deposit. c) presents a basalt clast thin section under plane-polarized light; d) presents a gneiss clast under both plane- and cross-polarized light.

Figure 3: Microphotographs of trachyte lava from the Sarcoui phreatomagmatic stage (without biotite reaction rim; left microphotographs), and the Sarcoui dome (with a noticeable reaction rim around biotite; right microphotographs). Top pictures are under plane-polarized light, and bottom pictures under cross-polarized light. Bt: biotite, Pl: plagioclase. Backscattered electron images of the biotite grain from the lava dome sample are presented in Figure 4b-c.

Figure 4: Characteristics of the biotite destabilization rims at Sarcoui lava dome. a-k panels are backscattered electron images, with h-i images obtained by modifying contrast and colors to better highlight phase relations. An attempt of reaction mass balance is presented (0.5 biotite + 0.5 melt => 0.63 K-feldspar + 0.18 titanomagnetite + 0.12 plagioclase + 0.04 clinopyroxene + 0.03 ilmenite + $melt_2$), it highlights that melt is present before and after the reaction, and that $melt_2$ is enriched in both Mg and K, and depleted in Fe. Representative compositions of the related phases are presented in Table 1. The high Mg# of the Cpx produced by the reaction is consistent with $melt_2$ being enriched in Mg. Panels b-c document the lava dome biotite grain presented in Figure 3.

Figure 5: Feldspar compositions in the studied dome and phreatomagmatic bomb (phreato) samples for Sarcoui dome. Left panel compare all data from the dome samples to all data from the phreatomagmatic bombs. Right panel compare the composition of phenocrysts, microlites, and crystallites.

Figure 6: Evolutionary model for Sarcoui volcano. Magma feeding both the phreatomagmatic and dome stages followed the same evolution and ascent conditions up to the shallow depth at which magma interacted with water during the phreatomagmatic stage. The optimal water:magma ratio triggering phreatomagmatic fragmentation is here schematized by the representation of a water-rich porous layer named "water table"; see White & Valentine (2016) for a discussion on this optimal ratio. The magma was quenched during

463 phreatomagmatism, whereas it slowly cooled during lava dome emplacement, resulting in
464 extended magma degassing and associated hydrous mineral (biotite) destabilization.

465

466 Table 1: Representative analysis of feldspar, biotite, and of the minerals forming the
467 breakdown reaction rims of biotite from Sarcoui samples. phreato: phreatomagmatic
468 bombs; FdK potassic feldspar; ilm: ilmenite; TiMgt: titanomagnetite; Cpx: clinopyroxene;
469 melt (800SAR2): melt used in the mass balance calculation as a reactant from Martel et al.
470 (2013) experiments at 800°C. The buck-rock composition provided by Martel et al. (2013) is
471 also presented.

472

473 Table S1: Sample list, type, and coordinates.

474

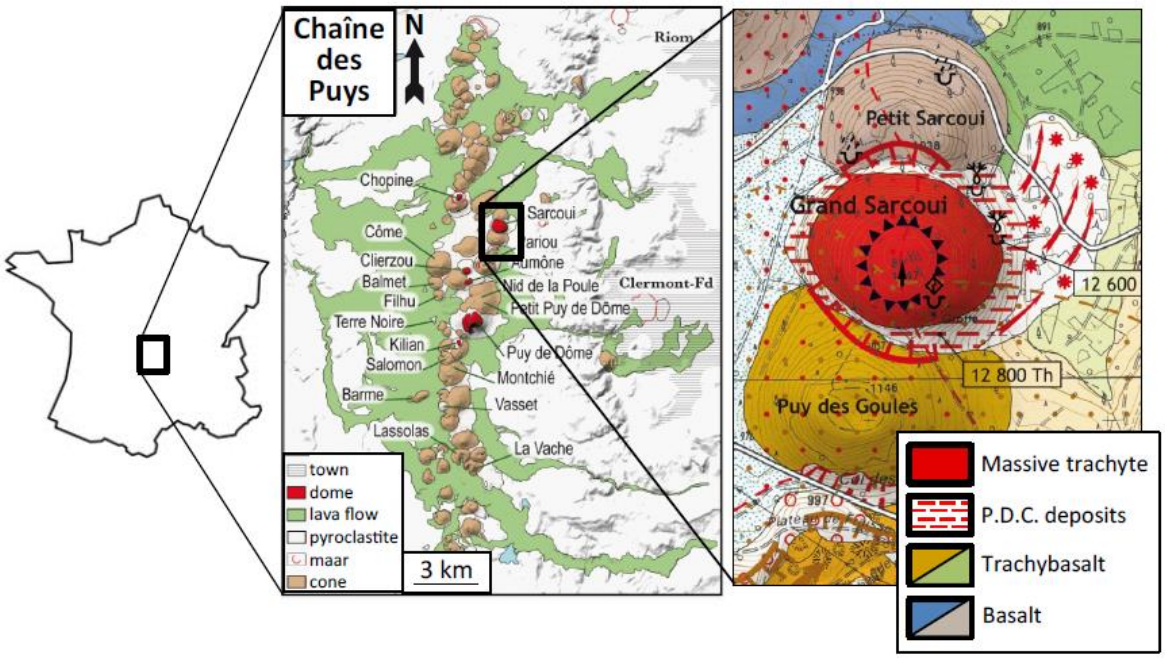

Figure 1

475

476

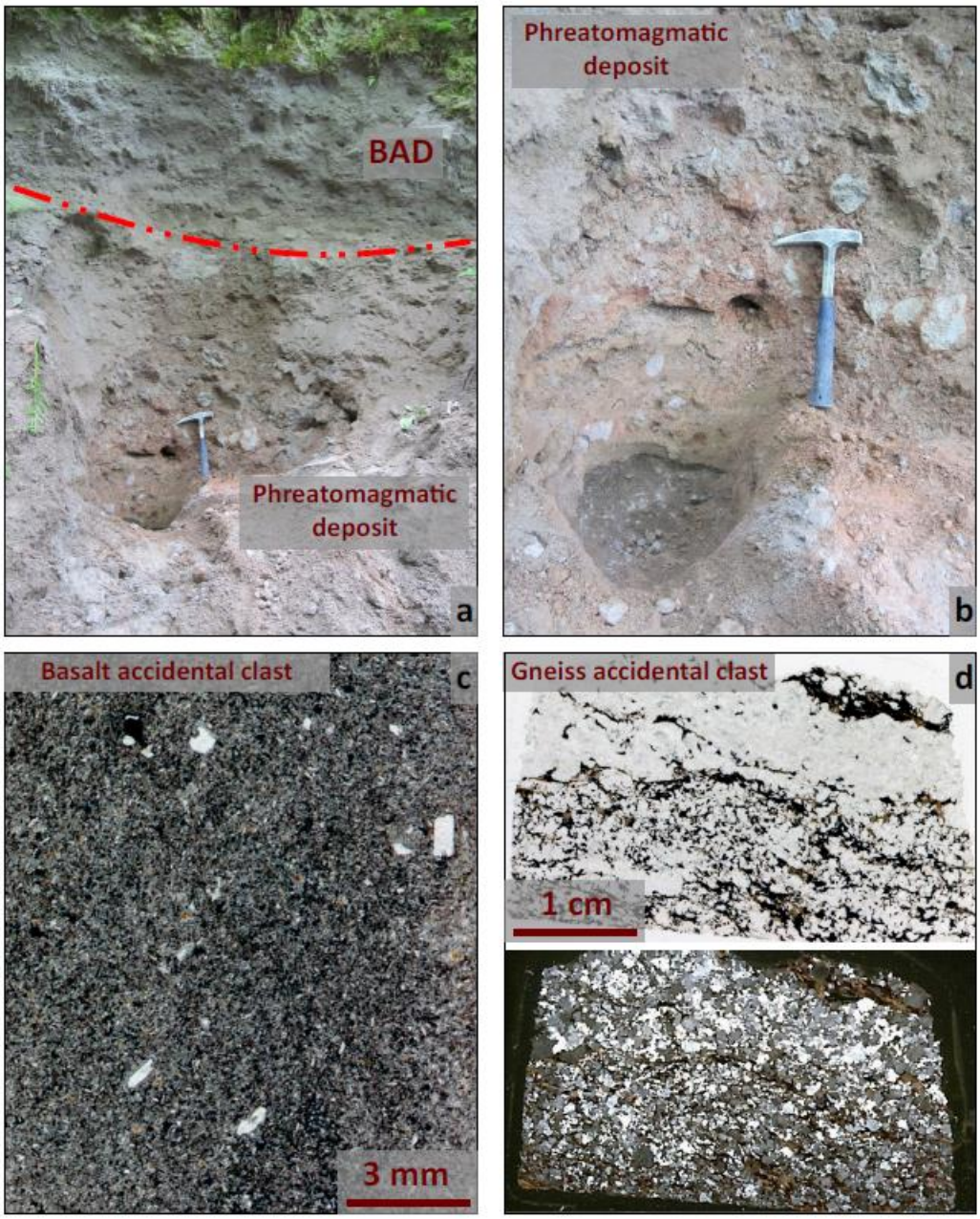

Figure 2

477

478

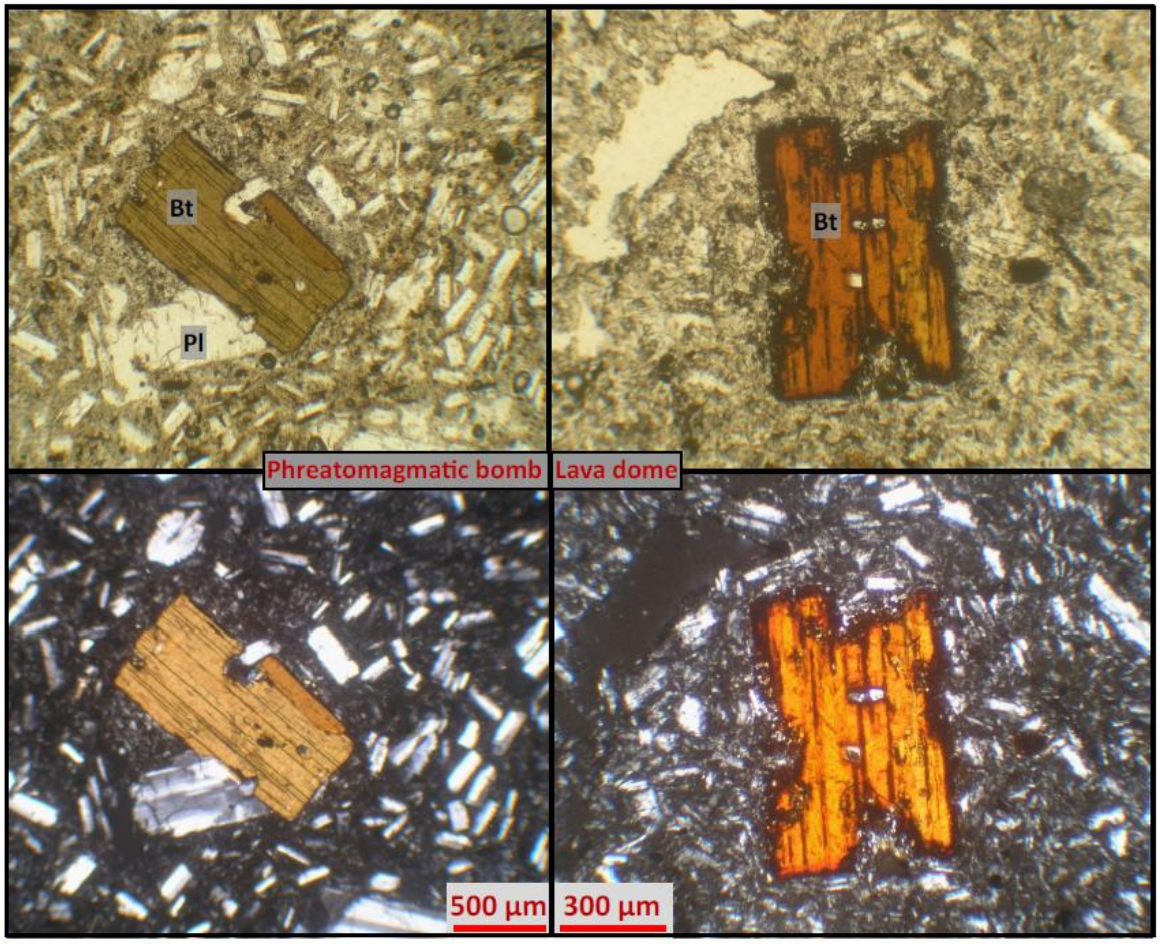

Figure 3

479

480

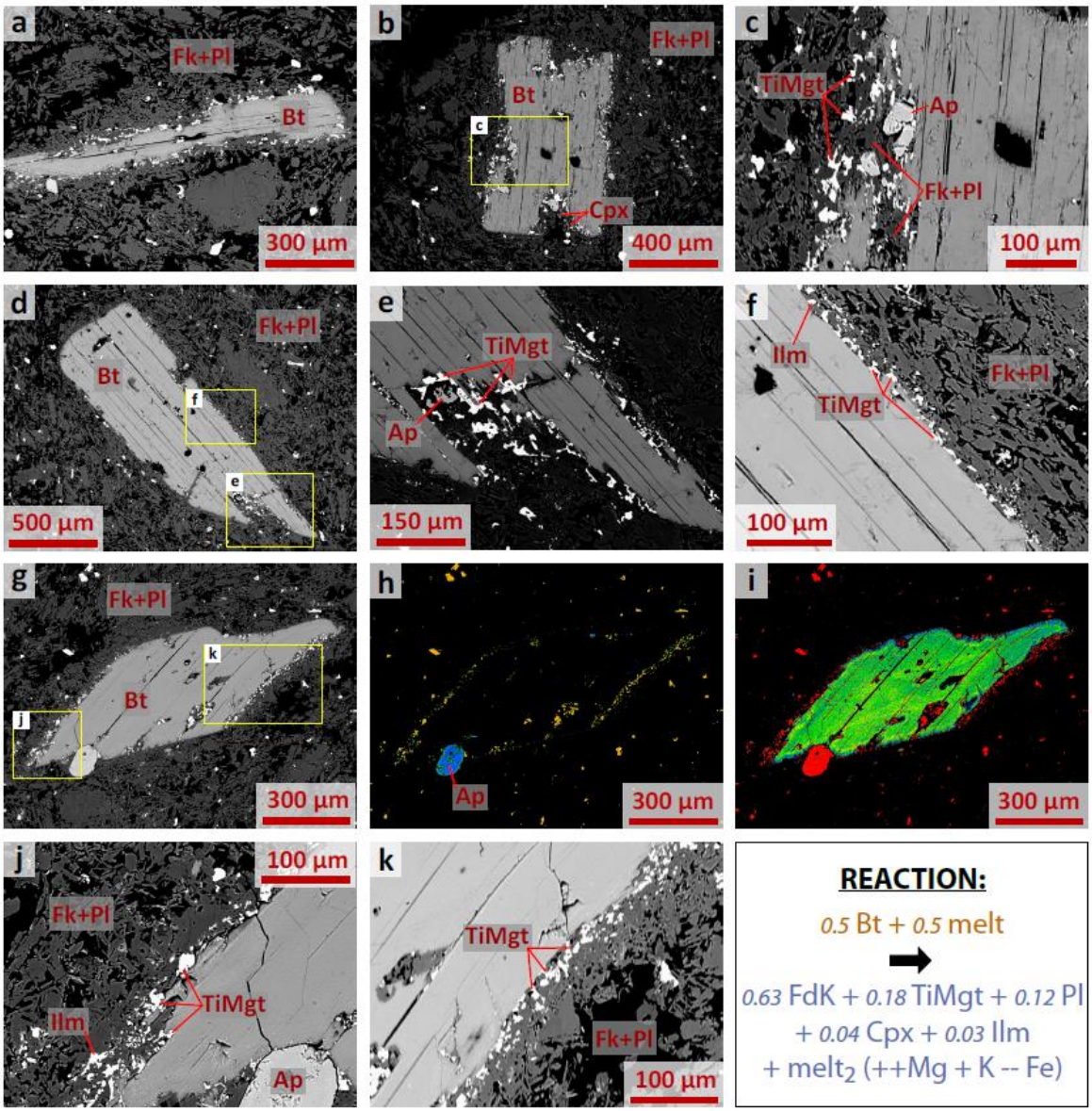

Figure 4

481

482

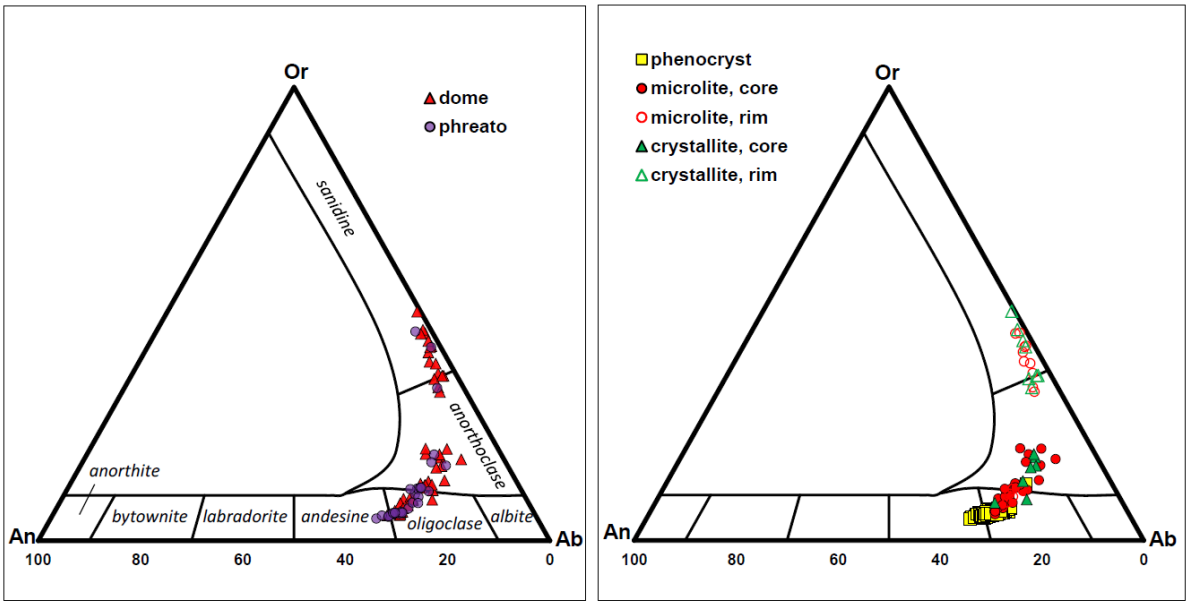
Or
dome
phreato
sanidine
anorthoclase
anorthite
bytownite
labradorite
andesine
oligoclase
albite
An
Ab
100
80
60
40
20
0
phenocryst
microlite, core
microlite, rim
crystallite, core
crystallite, rim

Figure 5

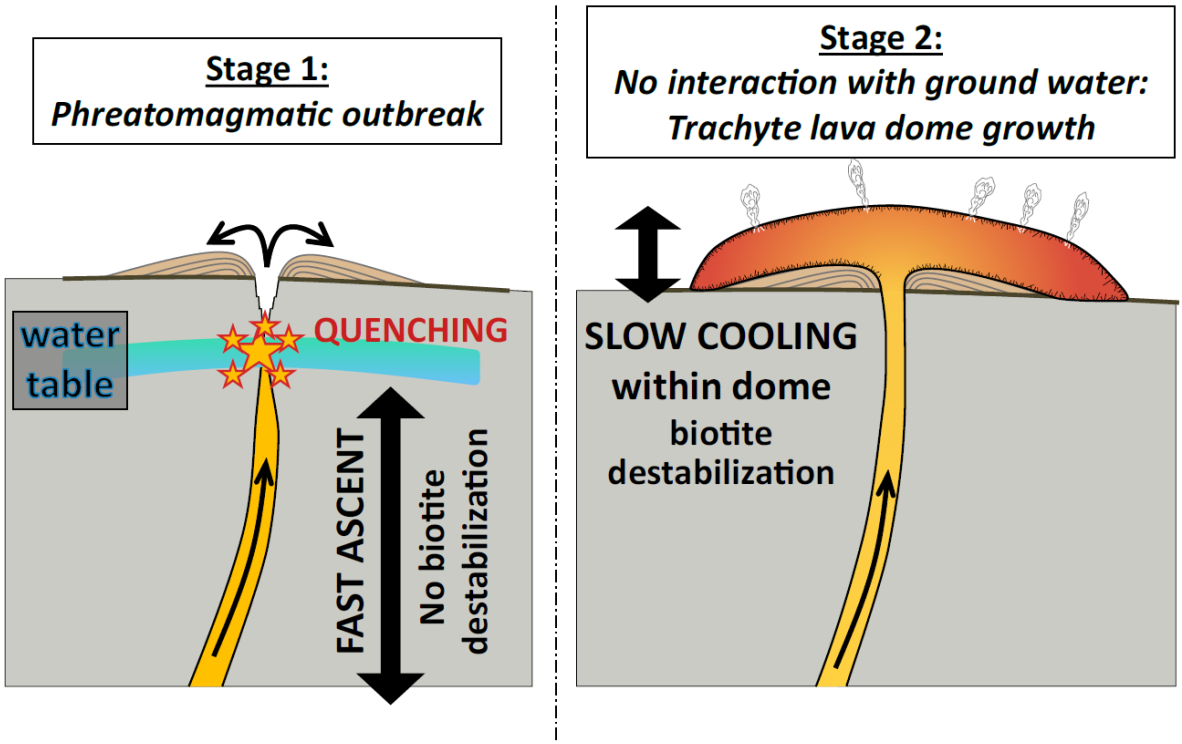

Figure 6

485

486

487 Table 1:

			n	SiO_2	Al_2O_3	TiO_2	CaO	Na_2O	K_2O	MnO	MgO	FeO	Cl	Total	*#Mg*	*An*	*Ab*	*Or*
Feldspar	Dome	phenocryst core	*8*	62.3	22.9	-	5.0	7.7	1.3	-	0.0	0.3	-	99.4		*24.5*	*67.9*	*7.6*
		+/–		*0.6*	*0.6*		*0.8*	*0.2*	*0.4*		*0.0*	*0.1*				*3.6*	*1.5*	*2.2*
		microlite core	*16*	63.3	22.0	-	4.0	7.8	2.0	-	0.0	0.3	-	99.4		*19.6*	*69.0*	*11.4*
		+/–		*1.4*	*1.0*		*1.2*	*0.3*	*0.8*		*0.0*	*0.1*				*5.7*	*2.1*	*4.6*
		crystallite core	*7*	64.3	21.4	-	3.3	7.9	2.4	-	0.0	0.4	-	99.7		*16.0*	*69.7*	*14.3*
		+/–		*1.4*	*0.8*		*0.9*	*0.3*	*0.7*		*0.0*	*0.1*				*4.4*	*1.6*	*4.0*
		microlite rim	*10*	66.3	18.7	-	0.6	6.4	6.9	-	0.0	0.4	-	99.4		*3.0*	*56.9*	*40.0*
		+/–		*0.5*	*0.5*		*0.2*	*0.3*	*0.8*		*0.0*	*0.1*				*1.2*	*3.2*	*4.3*
		crystallite rim	*6*	67.1	18.4	-	0.5	6.3	7.1	-	0.0	0.6	-	100.0		*2.3*	*56.1*	*41.6*
		+/–		*0.3*	*0.5*		*0.3*	*0.6*	*0.9*		*0.0*	*0.1*				*1.3*	*4.7*	*5.8*
	phreato	phenocryst core	*14*	61.5	23.4	-	5.7	7.6	1.0	-	0.0	0.3	-	99.5		*27.7*	*66.5*	*5.8*
		+/–		*0.4*	*0.4*		*0.4*	*0.2*	*0.1*		*0.0*	*0.1*				*1.7*	*1.3*	*0.4*
		microlite core	*9*	63.5	21.6	-	3.8	7.8	2.2	-	0.0	0.3	-	99.2		*18.4*	*68.9*	*12.7*
		+/–		*0.9*	*0.8*		*0.8*	*0.1*	*0.7*		*0.0*	*0.1*				*4.0*	*1.2*	*3.8*
		microlite rim	*7*	63.8	21.6	-	3.4	7.5	2.9	-	0.0	0.3	-	99.5		*16.5*	*66.2*	*17.3*
		+/–		*1.2*	*1.3*		*1.4*	*0.8*	*2.1*		*0.0*	*0.1*				*6.8*	*6.5*	*12.8*
		crystallite rim	*2*	66.8	18.6	-	0.7	6.4	6.4	-	0.0	0.6	-	99.4		*3.5*	*58.4*	*38.2*
		+/–		*0.1*	*0.2*		*0.3*	*0.0*	*1.0*		*0.0*	*0.1*				*1.7*	*2.9*	*4.5*
Biotite	dome		*14*	35.8	14.3	5.41	0.0	0.76	8.8	0.59	12.5	17.2	0.17	95.6	*56.4*			
				0.5	*0.6*	*0.12*	*0.0*	*0.06*	*0.2*	*0.15*	*0.2*	*0.5*	*0.10*	*0.5*	*0.9*			
	phreato		*14*	35.7	14.0	5.37	0.0	0.77	8.7	0.53	12.6	17.6	0.24	95.6	*56.1*			
	+/–			*0.4*	*0.3*	*0.29*	*0.0*	*0.05*	*0.1*	*0.10*	*0.2*	*1.2*	*0.42*	*0.8*	*1.8*			
Representative compositions of biotite's rim minerals		FdK		64.9	18.5	0.3	0.6	5.6	6.9	0.1	0.0	1.5		98.4				
		ilm		0.2	1.0	33.5	0.1	0.0	0.1	1.7	3.5	48.6		88.8				
		TiMgt		0.1	1.3	11.2	0.0	0.1	0.1	3.6	4.9	68.5		89.7				
		Cpx		54.9	0.7	0.3	19.4	1.2	0.1	2.9	17.6	3.8		100.8	89.2			
		melt (800SAR2)		66.6	17.3	0.4	1.6	6.8	4.7	0.2	0.3	2.2		100.0				
Bulk-rock (from Martel et al. 2013)				65.5	17.0	0.4	1.7	6.9	4.7	0.2	0.5	2.7	0.04	99.7				

488

489